Analysis of the failure micro-mechanisms

Contents

Abstract

The evolution of damage and the mechanisms responsible for ductile failure are identified in the TRIP steel sheet submitted to different stress states, using optical and scanning electron microscopy. Experiments are performed on tensile specimens and on disk specimens submitted to out-of-plane hemispherical punching, thereby covering stress states from uniaxial to equi-biaxial tension. For each specimen geometry, experiments have been interrupted prior to fracture at different stages of deformation: onset of through the thickness necking and 95%, 99% of the displacement at which fracture initiates. Micrographs of samples extracted from the deformed specimens permit to evaluate the material damage for increasing amounts of accumulated plastic strain, and identify rupture mechanisms. It is shown that the critical mechanism

---

[9] This Chapter is reproduced from: Dunand M., Mohr D. and Ravi-Chandar K., "Shear fracture of Advanced High Strength Steels: Mechanism Analysis and Micromechanical modeling". *Submitted.*

responsible for material failure is the localization of the plastic deformation in a shear band initiating at a grown and isolated void. The orientation of the fracture surface is controlled by the shear band direction.

6.1 Introduction

Damage mechanisms leading to ductile failure are generally described in terms of void nucleation, void growth and finally void linkage that form cracks. An extensive review of ductile fracture mechanisms can be found in Garrison and Moody (1987, [63]). Observation and characterization of damage mechanisms is traditionally done by means of optical and Scanning Electron microscopy. This destructive approach only gives access to two-dimensional information. High resolution tomography and laminography are now increasingly used for non-destructive three-dimensional observation of damage in metallic materials (e.g. Morgeneyer et al, 2008, [128]; Maire et al., 2012, [117]).

In this Chapter, attention is limited to studying the mechanisms leading to ductile failure under biaxial tension, i.e. plane stress states between uniaxial tension and equi-biaxial tension. A series of interrupted tensile experiments is performed on specimens extracted from TRIP780 steel sheets. A specimen with a central hole is used to study uniaxial tension, while notched flat specimens cover intermediate stress states in the vicinity of plane strain tension. In addition, interrupted punch experiments are performed to investigate the failure mechanism under equi-biaxial tension. Micrographs of specimens corresponding to different stages of loading prior to failure are analyzed in view of void nucleation and growth as well as localization of plastic deformation at the grain level. The experimental observations suggest that shear band formation is the governing failure mechanism under biaxial tension.

6.2 Macroscopic analysis: experiments and simulations

Different experiments are performed to shed some light on the fracture mechanism at stress states in the vicinity of biaxial tension. A finite element simulation

is performed of each experiment to provide access to the local stress and strain fields inside the specimen. The reliability of the numerical simulation and the underlying plasticity model is not demonstrated here as it is covered by previous publications on this material (Dunand and Mohr (2010, 2011, [48-50]) and Mohr et al. (2010, [122])), as well as in Chapter 5. Instead, we focus on describing the experimental and numerical results at the macroscopic level in the present section, before moving to the microscopic level in the sequel.

6.2.1   Notched tension experiments

Tensile experiments are performed on flat notched specimens (Fig. 6-1a). Specimens are 20mm wide in the shoulder area and feature a minimum width of 10mm at the center. The notch radius is R=6.65mm. Experiments are carried out under displacement control at a constant crosshead velocity of 0.5mm/min. Planar Digital Image Correlation (2D-DIC) is used to measure the relative displacement of the specimen boundaries and the displacement field at the center of the gage section.

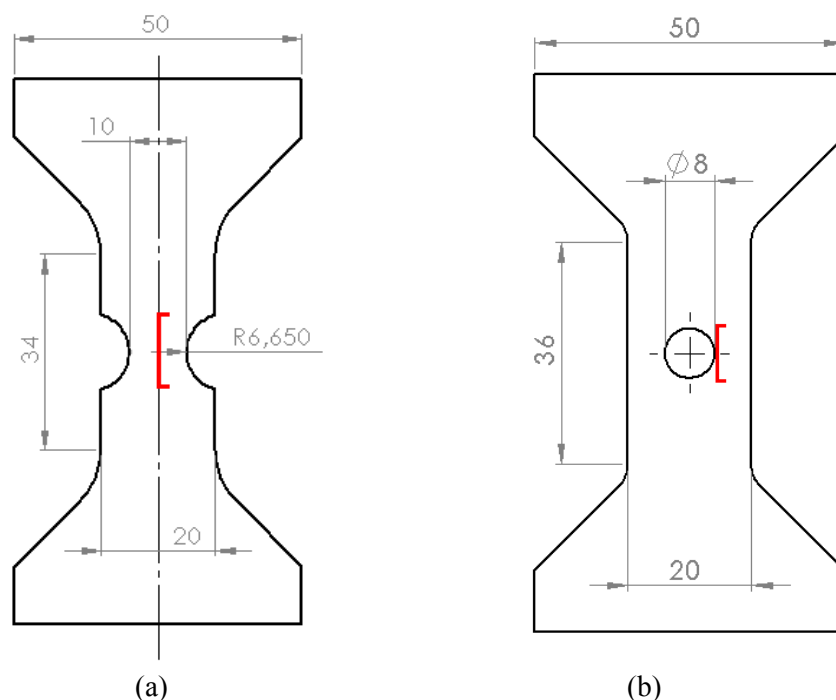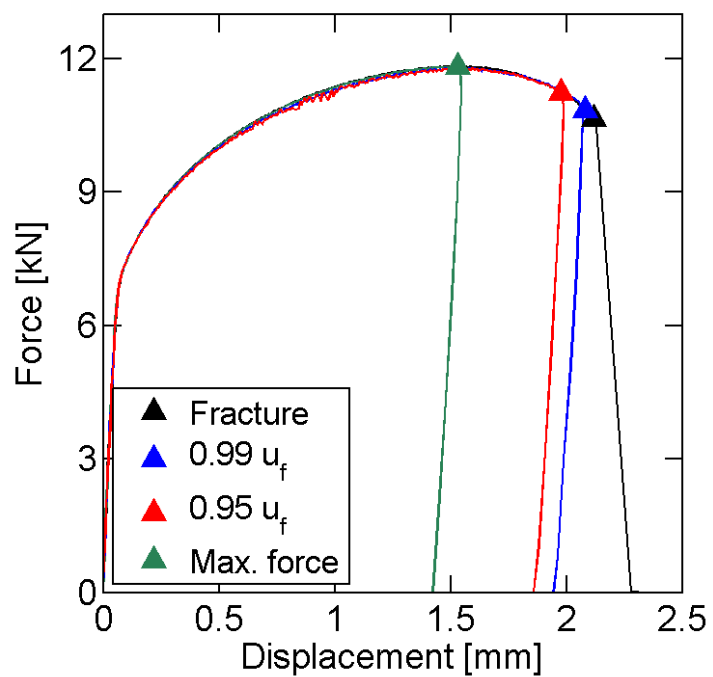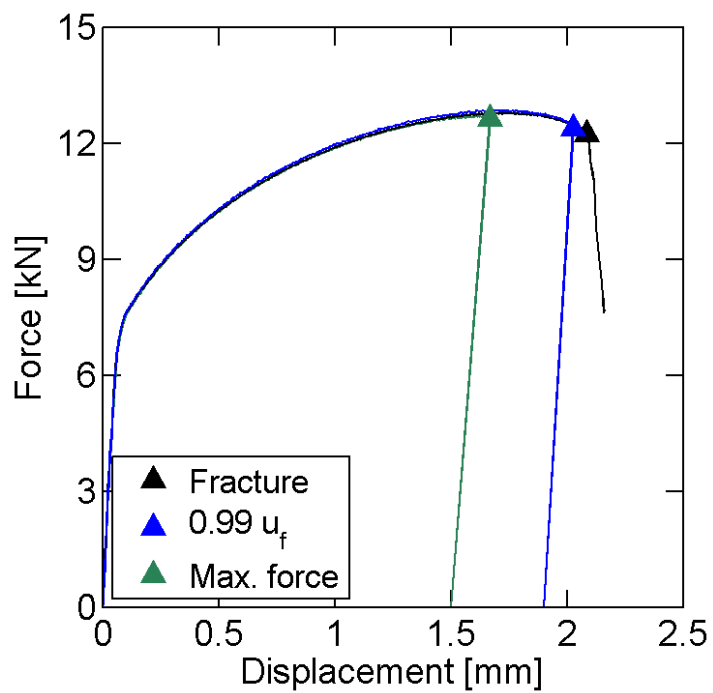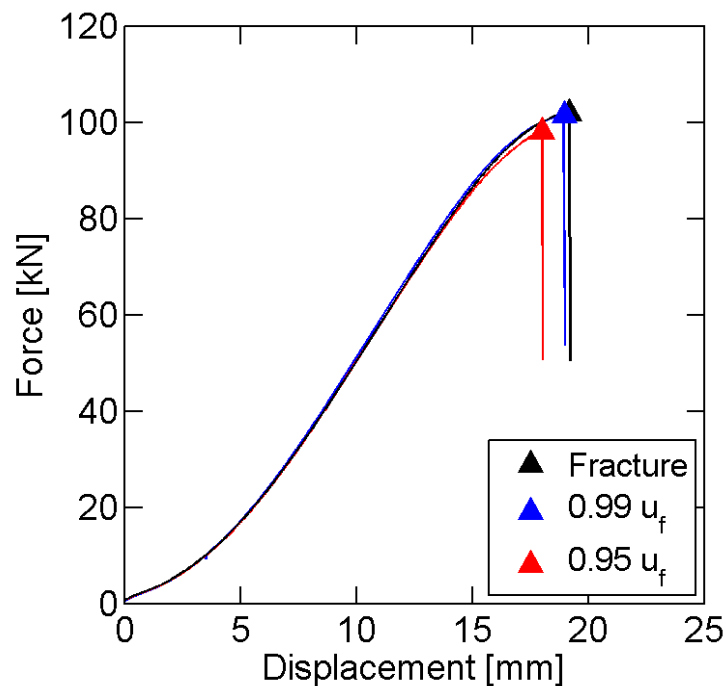(a)   (b)

Figure 6-1: Tensile specimens with (a) a notch radius 6.65mm and (b) tensile specimen with central hole. Red marks depict the position from where micrography samples are extracted.

(a)

(b)

(c)

Figure 6-2: Force displacement curves of the (a) notched tensile experiment, (b) central hole tensile experiment and (c) punch experiment.

The measured force-displacement curve is depicted in black in Fig 6-2a. A force maximum is reached before fracture occurs, roughly corresponding to the instant of the onset of through-the-thickness necking. Beyond the onset of necking, steep gradients in the stress and strain fields develop both in-plane and through-the-thickness at the center of the specimen gage section (Fig. 6-3).

The plane stress condition prevail up to the onset of through-thickness necking. Thereafter, a stress in specimen thickness direction builds up. The corresponding plots of the estimated loading paths at the specimen center, i.e. the evolution of the equivalent plastic strain as a function of the stress triaxiality and the Lode angle parameter, therefore show a pronounced kink associated with necking followed by an increase in stress triaxiality and a decrease in the Lode angle parameter (Fig. 6-4). The reader is referred to Dunand and Mohr (2010, [48]) for more details on the numerical model.
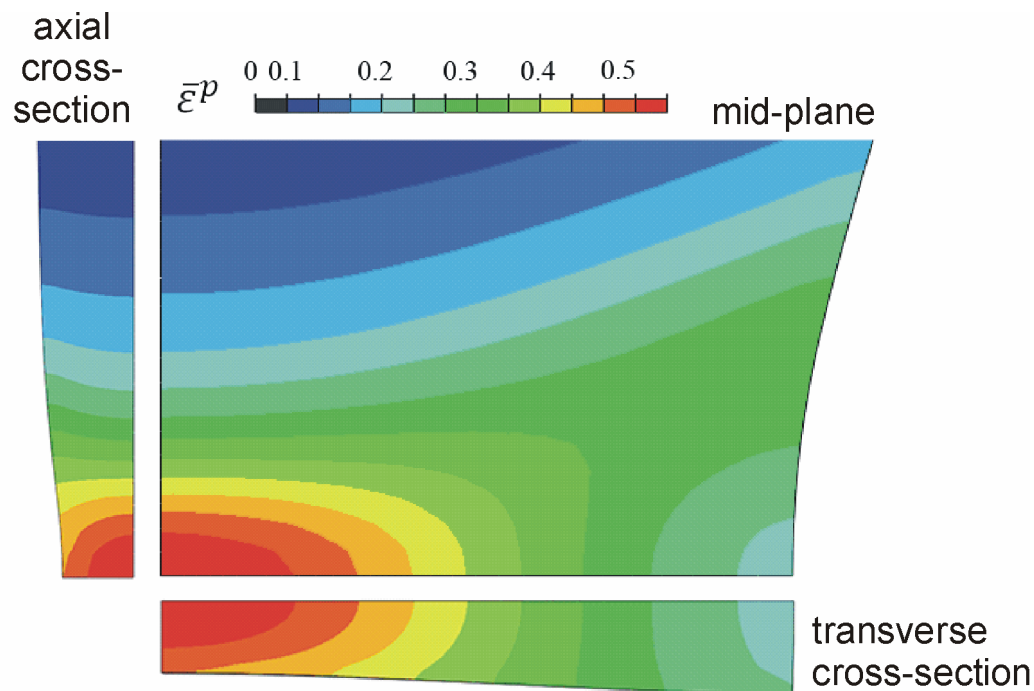
Figure 6-3: Contour plot of the equivalent plastic strain at the instant of the onset of fracture in a notched specimen.

In addition to the monotonic experiment all the way to fracture, the experiment is repeated for additional specimens, but interrupted prior to fracture at different stages of deformation: maximum of force; 95% and 99% of the displacement at which fracture initiates. Due to the excellent repeatability of the experiments for the material at hand, the corresponding force-displacement curves lie on top of each other (Fig. 6-2a). The end points of the interrupted experiments are therefore highlighted by a triangle symbol in Fig. 6-2a and 6-4.

6.2.2   Tension on a specimen with a central hole

In close analogy with the experimental program on the notched tension specimen, experiments are performed on a tensile specimen with a central hole (Fig. 6-1b). The hole has a diameter of 8mm while the ligaments to the left and right of the hole are each 6mm wide. Following exactly the same procedure as for the notched specimen, a monotonic experiment is performed all the way to fracture, followed by a series of
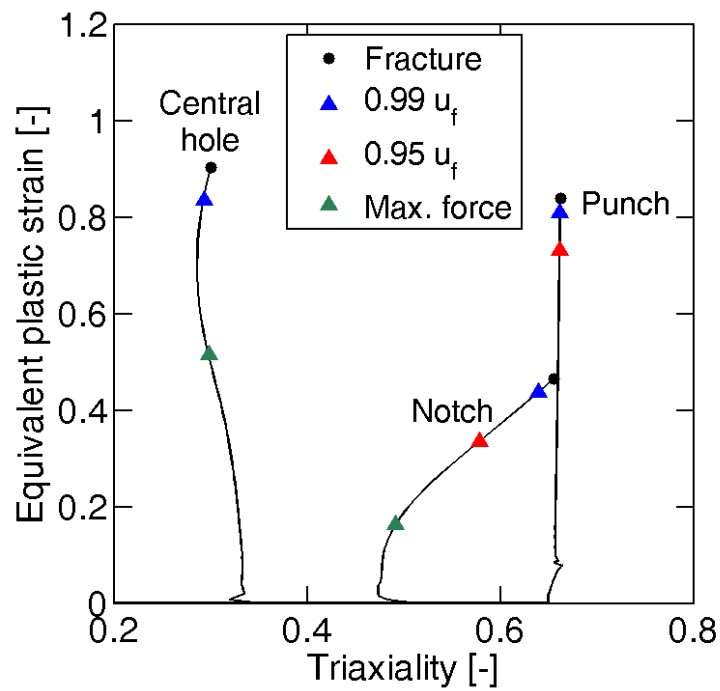
(a)
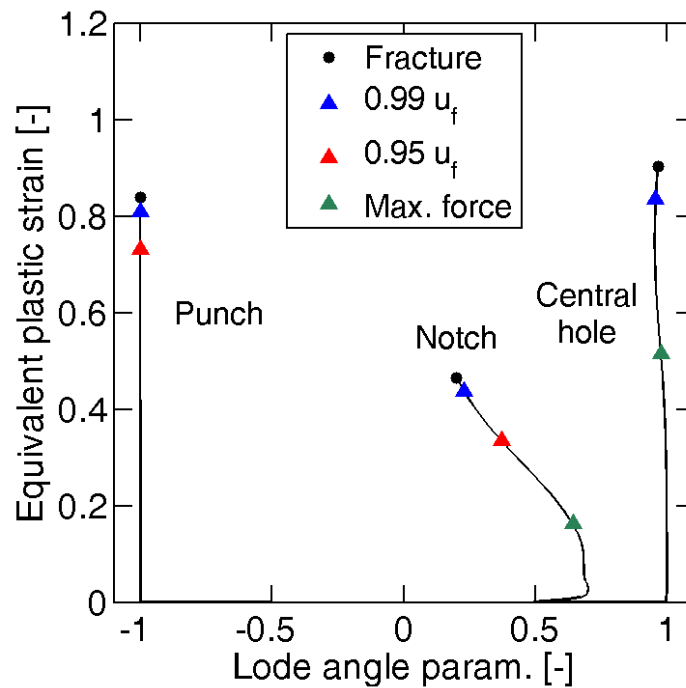
(b)

Figure 6-4: Loading paths to fracture. (a) Evolution of equivalent plastic strain versus stress triaxiality and (b) evolution of equivalent plastic strain versus Lode angle. Solid points depict the onset of fracture.

interrupted experiments ending at maximum of force and 99% of the displacement of total failure, respectively. Corresponding force-displacement curves are shown in Fig. 6-2b.

The cracks are assumed to initiate near the boundary of the central hole. The corresponding finite element simulation shows that through-thickness necking occurs in the hole ligaments, with the strongest thickness reduction of up to 38% at a distance of 0.9mm from the hole boundary. The evolution of the stress state at an integration point located at the specimen mid-plane near the hole boundary is shown in Fig. 6-4. Due to the proximity to the hole boundary, the stress state remains close to uniaxial tension all the way to fracture, i.e. the stress triaxiality and Lode angle parameter are close to 0.33 and 1.0, respectively. Selected views of the deformed FEA mesh at the instant of onset of fracture are shown in Fig. 6-5 with a contour plot of the axial plastic strain.
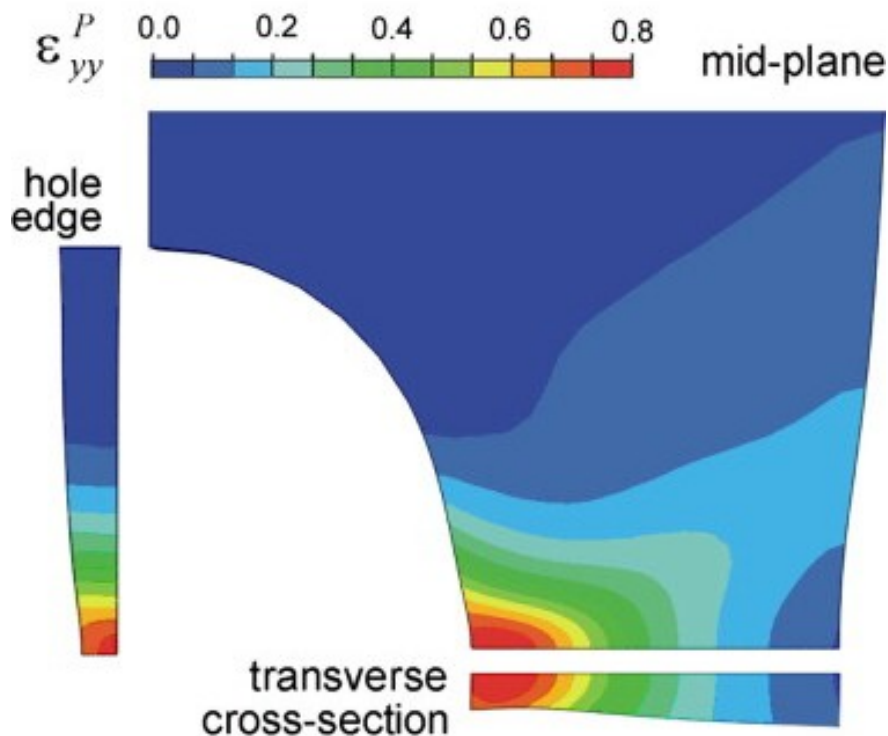

Figure 6-5: Specimen with a central hole: contour plot of plastic axial strain at the instant of the onset of fracture.

6.2.3   Punch Experiment

In order to characterize the material response for equi-biaxial tension, a sheet specimen is clamped on a circular die and subsequently loaded through a hemispherical punch. The punch and die have a diameter of 44.5mm and 100mm, respectively. The clamping pressure is applied through eight M10-12.9 screws. The experiment is carried out on a screw-driven universal testing machine (MTS, Model G45) at a constant punch velocity of 5mm/min. In order to limit the effects of friction, a stack of six oil-lubricated 90μm thick Teflon layers is put between the specimen and the punch during each test. Three-dimensional Digital Image Correlation is used to measure the out-of-plane deformation of the specimen. The applied force versus punch displacement curve is depicted in black in Fig. 6-2c; it increases monotonically until a sharp drop in the force level is observed at the instant of the onset of fracture. Fracture occurs at the top of the dome, where the stress state is close to equi-biaxial tension.

As for the tensile experiments, we also carry out interrupted punch experiments where loading was stopped at 95% and 99% of the punch displacement at which fracture initiates. Corresponding superposing force-displacement curves are shown in Fig. 6-2c with triangle-symbols indicating the points of interruption. The accompanying finite element simulations shows the absence of through-thickness necking. As a result, the loading path to fracture remains more or less proportional, i.e. both the stress triaxiality and the Lode angle parameter remained constant at 0.66 and -1.0, respectively.

6.2.4   Dependence of the strain to fracture on stress state

The results from the above experiments along with the computational analysis provide insight into the stress state dependency of the strain to fracture. Here, the "strain to fracture" is defined as the largest achievable macroscopic strain prior to the formation of cracks or narrow bands of localization of plastic deformation. This definition is very useful from an engineering point of view. From a physical point of view, it might be more meaningful to define the strain to fracture at smaller length scale. For instance, in polycrystalline materials, it could be associated with the plastic deformation at the grain level up to the point of micro-crack formation. Clearly, the use

of the latter definition would require more involved material models that can predict the strains at the grain level.

Taking a purely phenomenological macroscopic approach (see discussion in Section 2.2), stress triaxiality and Lode angle parameter dependent damage indicator models have been developed recently to describe the effect of stress state on the strain to fracture (e.g. Bai and Wierzbicki, 2010, [7]; Mohr and Marcadet, 2012, [125]). For biaxial tension, these models predict a minimum in the strain to fracture for transverse plane strain tension, while the strain to fracture is supposed to increase monotonically towards the respective limiting cases of uniaxial tension and equi-biaxial tension. It is the goal of the subsequent two sections, to provide a physics-based explanation of this characteristic drop in the strain to fracture for plane strain tension.

6.3   Fractographic analysis

6.3.1   Sample preparation

Cross-sectional cuts are prepared from the tested specimens for microscopic inspection. For the tensile experiments (notched and central hole specimens), the observation plane is the one containing the axial and thickness directions. A red solid line in Fig. 6-1 indicates the projection of the observed cross-sections on the specimen surface. For the punch experiment, the observation plane includes the thickness and transverse sheet direction, since the first cracks always formed parallel to the sheet rolling direction.

The sheet cutting is done using a wire saw. The samples preparation follows closely the procedure described in the Metals Handbook vol.8 (1990, [5]). The samples are first mounted in a conductive phenolic mounting compound filled with aluminum particles. They are then ground and polished. The final polishing step is performed with a $1\mu m$ diamond paste. Etching is finally performed using a 2% Nital solution.

## 6.3.2   Microscopic observations of polished cross-sections

A series of micrographs of the notched tensile specimens is shown in Fig. 6-6 as recorded with the Back-Scattered Electron (BSE) detector of a *FEI XL40* scanning electron microscope operating at $15kV$. According to our finite element analysis, the corresponding accumulated equivalent plastic strains at the specimen center are: $\bar{\varepsilon}^p = 0.17$ (maximum force, Fig. 6-6a), $\bar{\varepsilon}^p = 0.34$ (95% displ., Fig. 6-6b) and $\bar{\varepsilon}^p = 0.44$ (99% displ., Fig. 6-6c).

At maximum force (Fig. 6-6a), the specimen already exhibits noticeable damage in the form of voids. The area fraction of voids is about 4×10^{-3} in Fig. 6-6a, while virtually no voids are visible in the undeformed material (Fig. 1-1). The position of the voids suggests that they nucleated at the ferrite/martensite and/or ferrite/austenite grain boundaries. Strain incompatibilities between the different phases may induce more rapid debonding at the phase interfaces (Jacques et al., 2001, [87]). Moreover, most of the visible voids are aligned parallel to the loading direction (which also coincides with the sheet rolling direction). Lorthios et al. (2010, [114]) observed similar nucleation patterns in TWIP steels by means of x-ray tomography. Note that the undeformed material shows segregation bands of austenite (Fig. 1-1), which seem to be favored sites for void nucleation. Some voids have also nucleated away from the segregation bands at apparently random locations in the specimens.

Figure 6-6b ($0.95u_f$) shows a polished cross-section for significantly higher equivalent plastic with an estimated maximum of $\bar{\varepsilon}^p = 0.34$ at the specimen center. At this stage of deformation, the area fraction of voids has increased to about 7.4×10^{-3}. However, it is important to note that the average size of the voids is very similar to that of the voids observed at maximum force. In other words, the measured increase in void volume fraction is not due to void growth. Instead, it is due to additional void nucleation. Based on x-ray tomography quantitative observations made on a DP600 steel sheet and its phase constituents, Maire et al. (2008, [116]) and Bareggi et al. (2012, [12]) also concluded that the average void diameter does not increase during straining, while additional damage is mainly due to the nucleation of new cavities. At $0.95u_f$, the observed void alignments are longer than those at maximum force. Voids
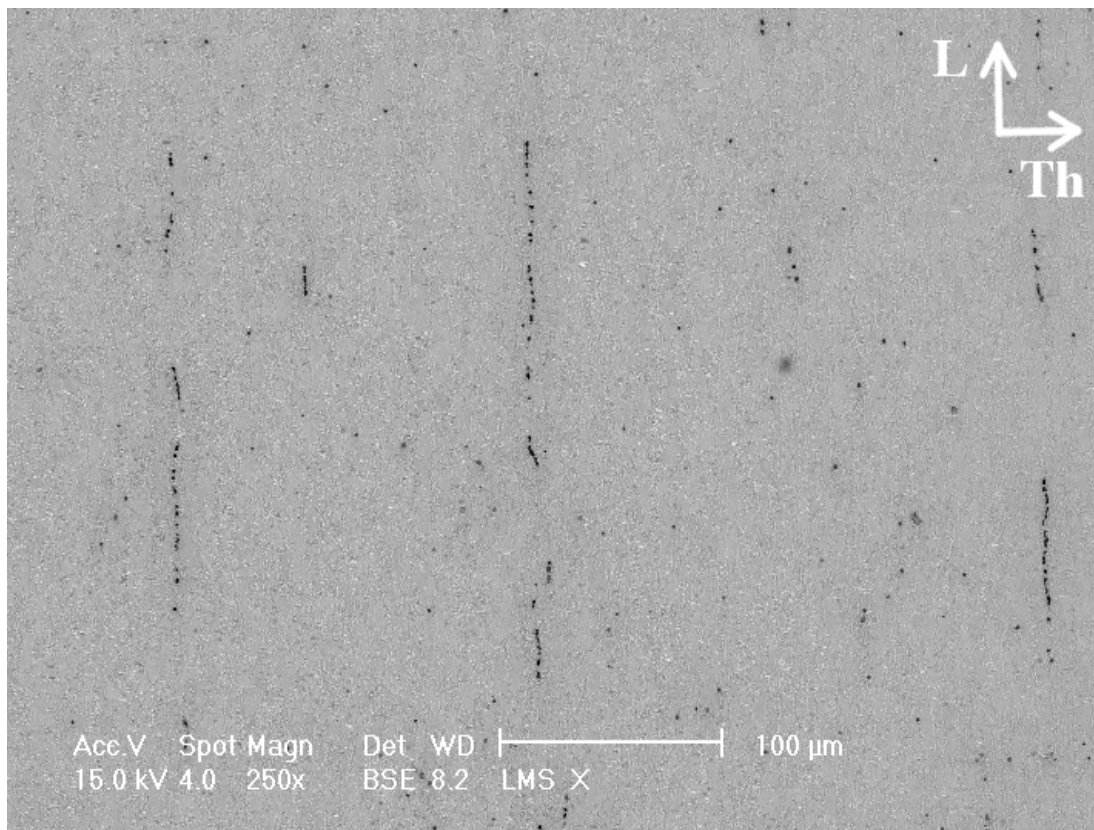
(a)
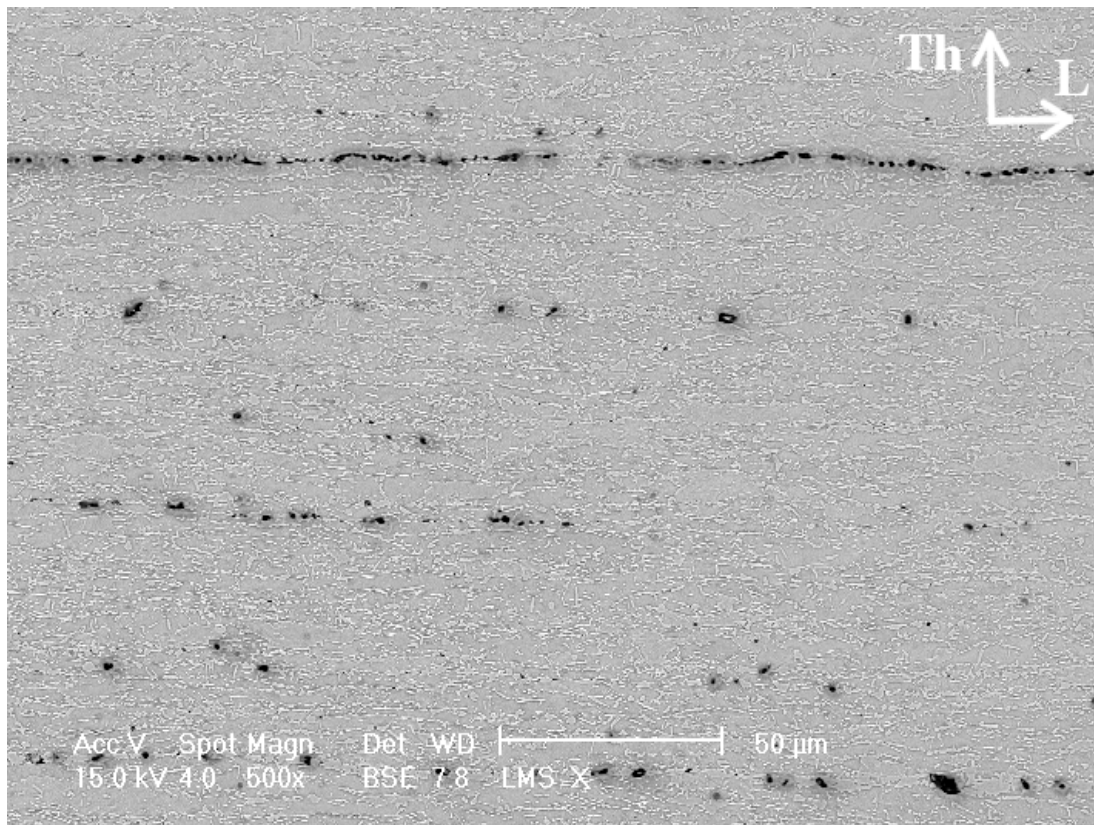
(b)
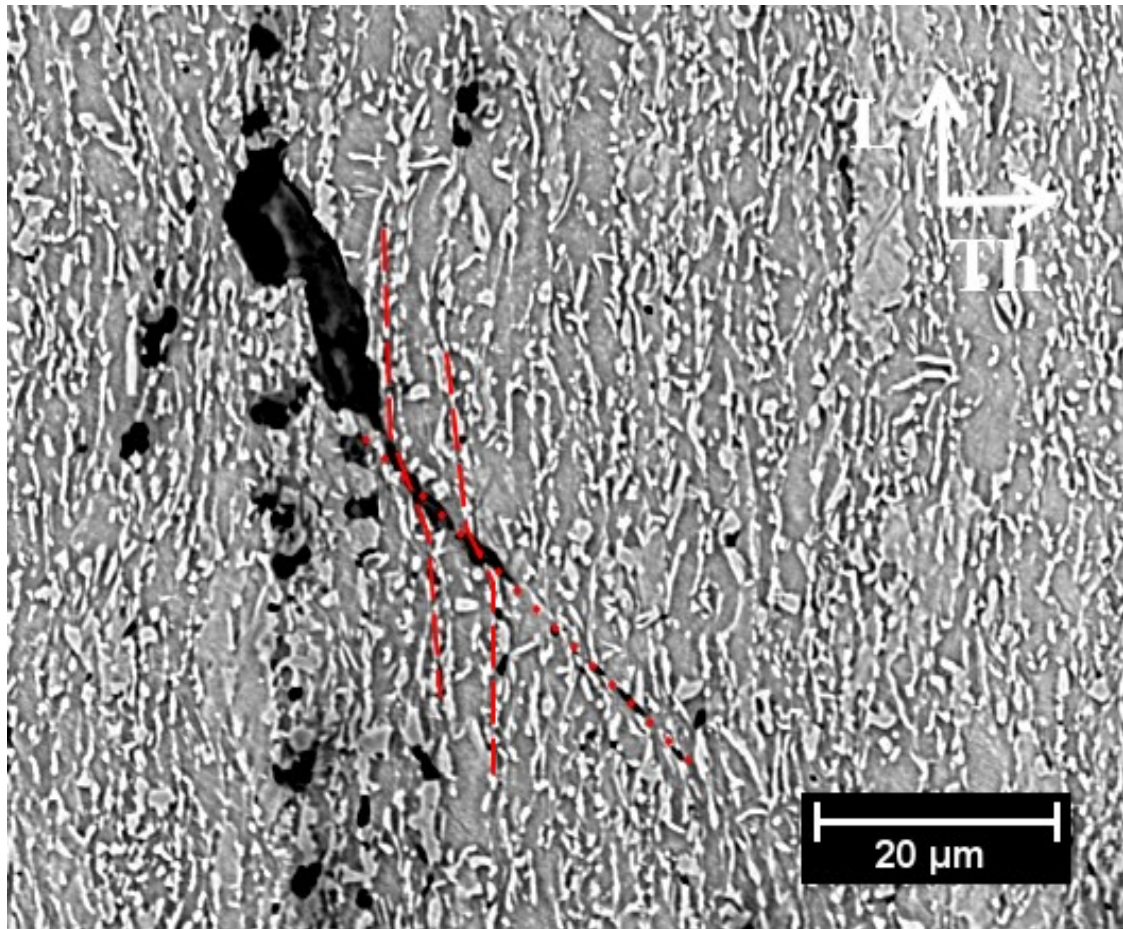
(c)

Figure 6-6: SEM micrographs from notched tensile experiments interrupted at (a) the maximum of force, (b) 95% of the displacement to fracture and (c) 99% of the displacement to fracture. The *L* and *Th* orientations correspond to the specimen loading direction and through-the-thickness direction, respectively.

seem to nucleate at both ends of the alignments. Void coalescence is also observed among voids within the same alignment, thereby forming microcracks parallel to the loading direction.
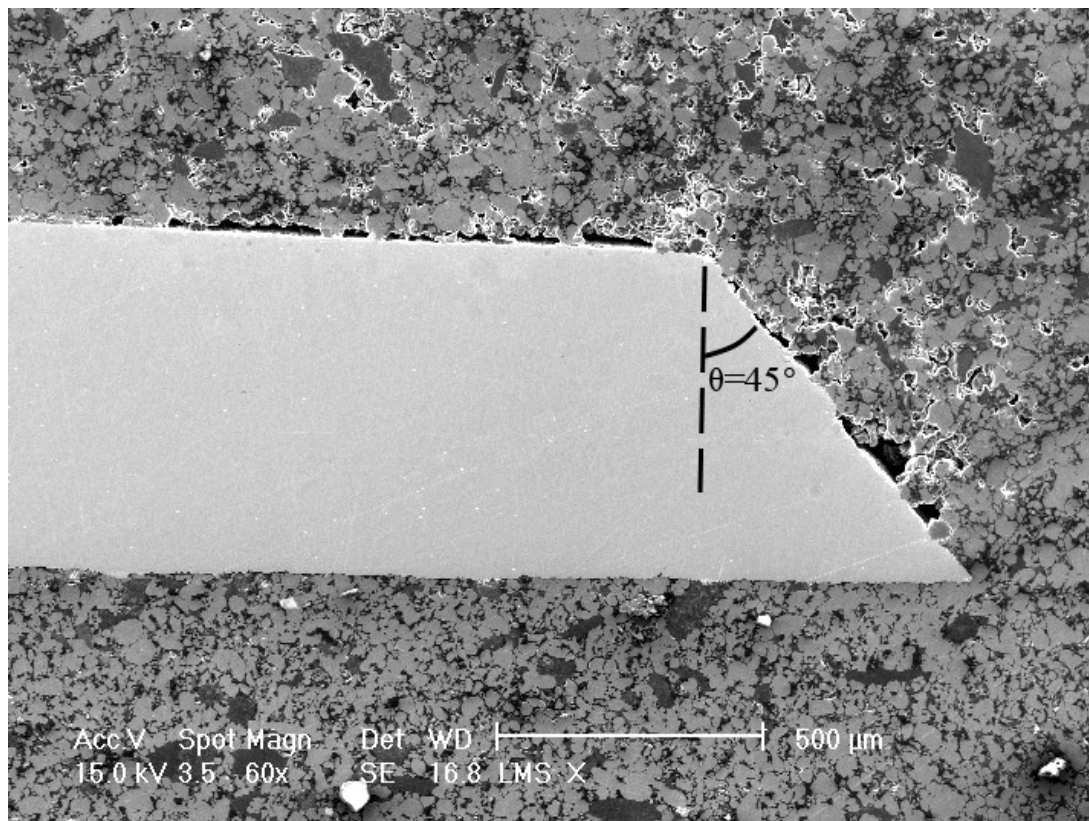
At 99% of the displacement to fracture, the observed mesostructure is similar to that at 95% of the displacement to fracture. However, at a higher magnification, the inspection of martensite grain bands (bright phase in Fig. 6-6c) shows signs of shear cracks. The martensite grains are organized in more or less straight bands along the
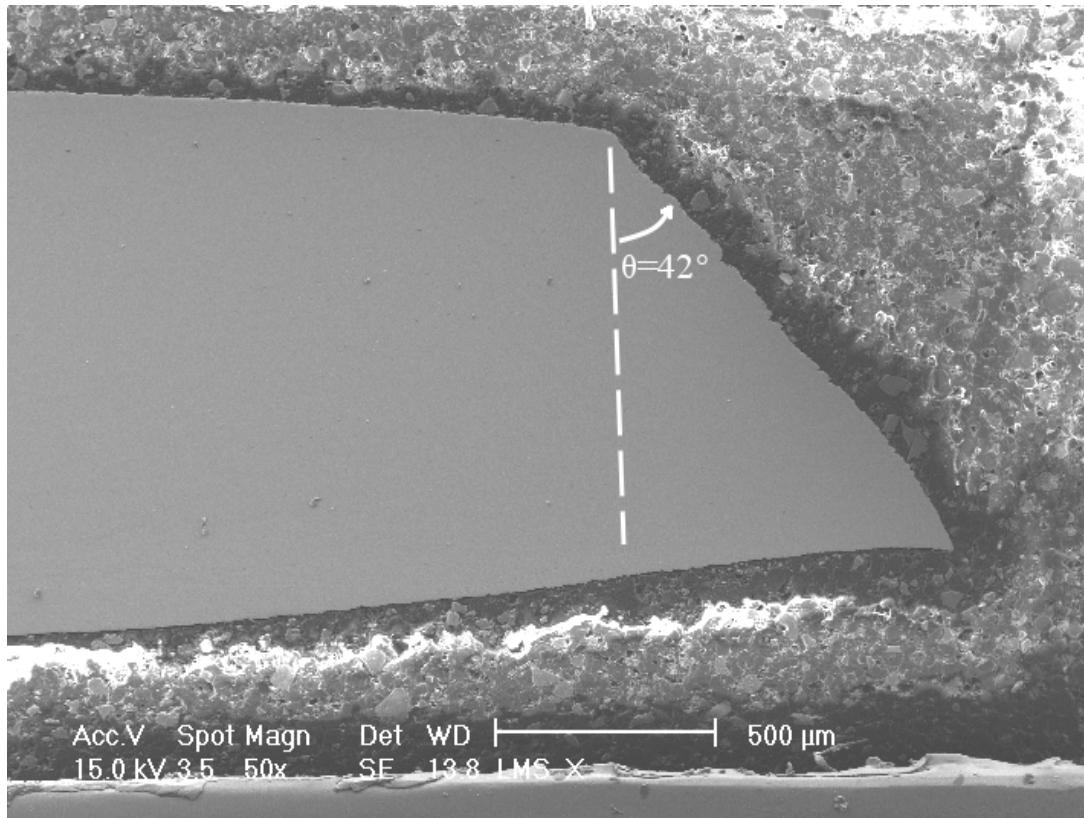
(a)
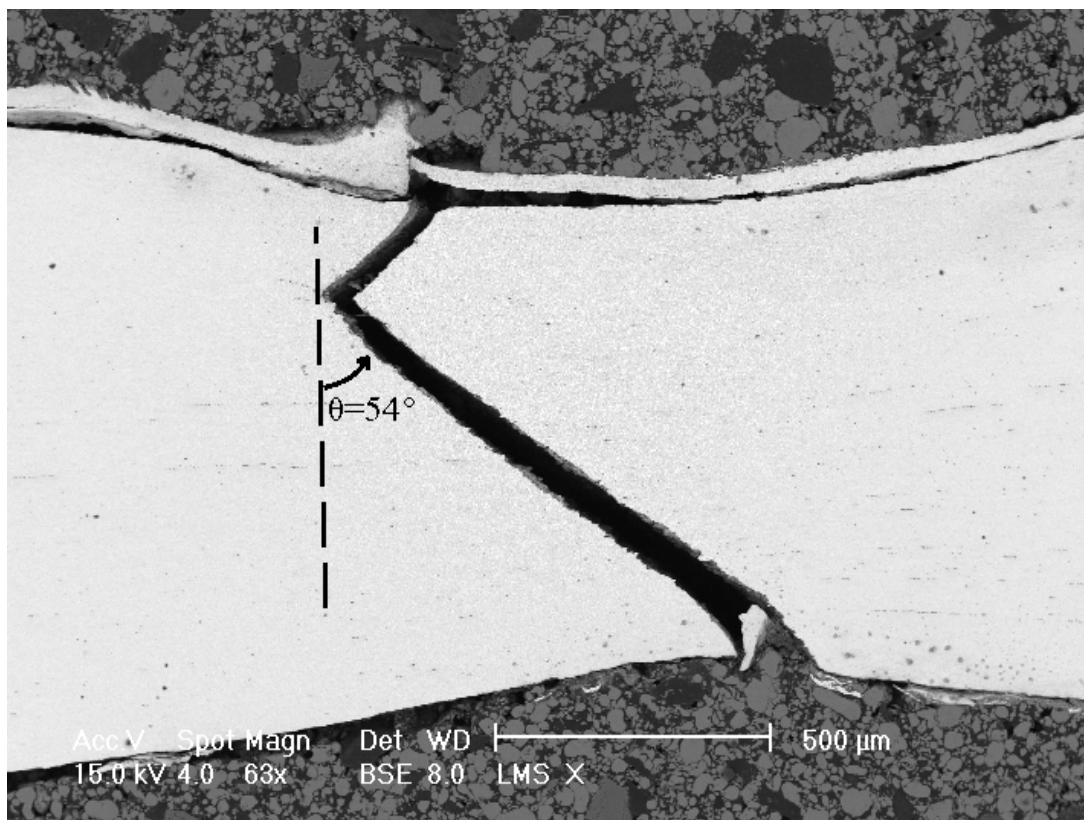
(b)

(c)

Figure 6-7: Cross sections of post-mortem specimens of (a) notched tensile experiment, (b) central hole experiment and (c) punch experiment.

rolling direction. Two such bands have been highlighted by red dashed lines in Fig. 6-6c. Prior to the fracture of the entire specimen (i.e. at 99% displ.), a tangential and normal discontinuity becomes apparent in the martensite bands. Figure 6-6c also shows a large hole at the top left which is disregarded because we think that it is just the trace of grains that have been torn out during polishing.

We note that remarkably similar observations are made when analyzing the corresponding cross-sectional cuts for tension with a central hole and even for the punch specimen. The corresponding micrographs of interrupted specimens are therefore not shown for conciseness. The longitudinal cross sections of the fractured notched and punch specimens all show straight slanted cracks (Fig. 6-7). In particular, the fracture surface is inclined at an angle of about 45° with respect to plane of the sheet. The only
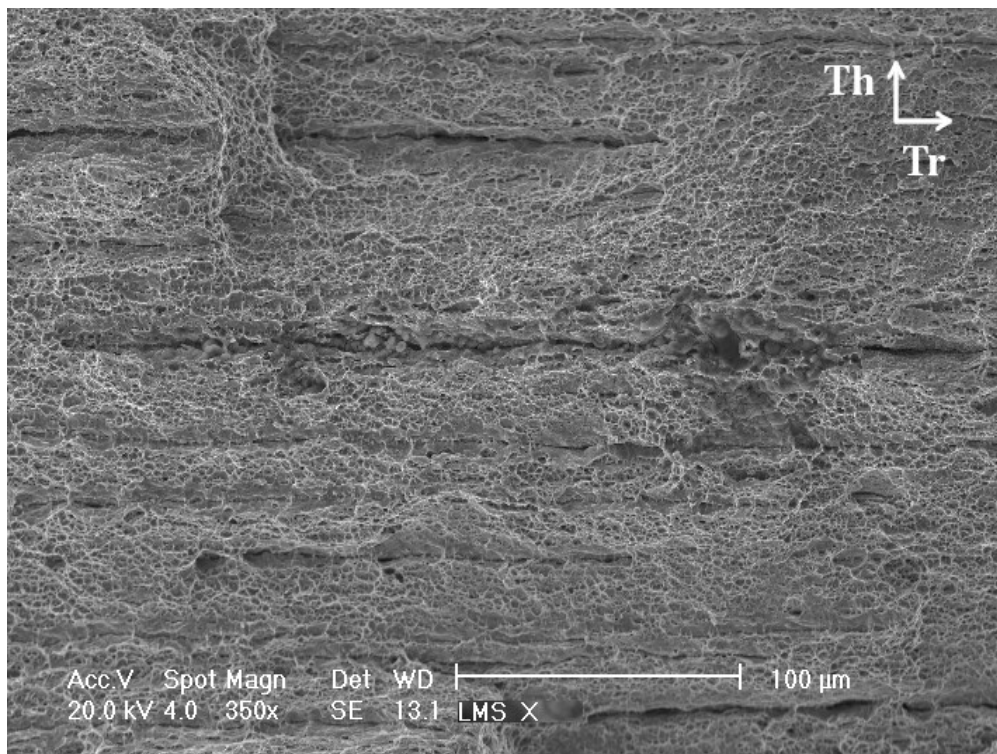
(a)
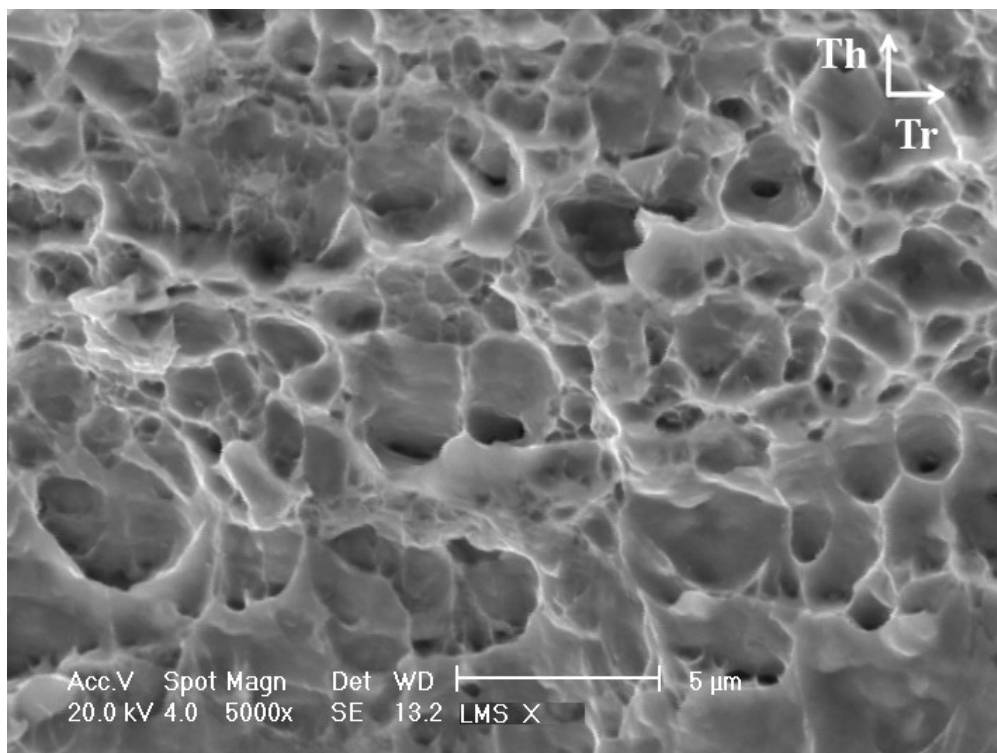
(b)

Figure 6-8: SEM fractographs from a broken notched tensile specimen. The *Th* and *Tr* orientations correspond to the through-the-thickness and specimen transverse directions, respectively.

exception is the central hole specimen, which features a V-shaped fracture surface (Fig. 6-7b).

6.3.3   Fracture surfaces

SEM fractographs from a notched tensile specimen are presented in Fig. 6-8. The fracture surface presents a dimple pattern with a dimple size of about $2\mu m$ (Fig. 6-8b). The eccentricity of the black apex of the dimples with respect to the bright circumference (Fig. 6-8b) suggests that the ellipsoidal dimples are inclined towards the thickness direction. At a smaller magnification (Fig. 6-8a), the fracture surface features continuous dark lines of narrow valleys that are parallel to the specimen surface. It resembles a laminate with multiple layers of $50\mu m$ to $100\mu m$ thickness. The layer thicknesses are similar to the distances between the void bands observed in the cross-sectional cuts. It is speculated that these valley lines corresponds to the intersection of the crack surface with the void necklaces.

6.3.4   Effect of strain rate on damage

Even though technological solution are available to perform interrupted experiments in Split Hopkinson Bar systems (e.g. Nemat-Nasser et al., [134]), it has not been implemented as part of this thesis. Damage mechanisms taking place at high strain rate are thus not formally identified. However, fracture surfaces and cross-sections of post-mortem specimens submitted to high strain rate loadings are similar to those describes hereinabove. It is therefore assumed that damage mechanisms are comparable at low and high strain rates.

6.4   Mechanical interpretation of the observations

Based on the above observations, the following comments with regards to the mechanism leading to ductile fracture under biaxial tension can be made:

1. Voids nucleate at ferrite/martensite and ferrite/austenite grain boundaries, preferably along alignments parallel to the specimen loading direction

Nucleation takes place before necking, i.e. at zero out-of-plane stress. At this stage, the plastic strains are small ($\bar{\varepsilon}^p < 0.2$) as compared to those reached at the onset of fracture ($\bar{\varepsilon}^p > 0.45$).

2. The void volume fraction increases mostly because of new nucleations (and not due to the growth of existing voids).

3. Through-thickness necking is just a structural deformation mode which localizes the deformation to a small zone within the specimen. At the length scale associated with necking (sheet thickness), the material can still be considered as a homogenous continuum.

4. The local increase in stress triaxiality due to necking has no noticeable effect on the size of the voids. Furthermore, a similar void size is observed for tension with central hole (triaxiality of 0.33), notched tension and in a punch experiment (triaxiality of 0.66).

5. Coalescence occurs within void alignments (necklace mechanism) thereby forming microcracks parallel to the specimen loading direction. However, it appears that those microcracks and voids do not compromise the material's load carrying capacity along the axial direction.

6. Voids acts as material imperfections that trigger the localization of the plastic flow into a narrow band of localized plastic deformation. At this stage, a homogeneous description of the material is expected to become invalid. Due to the 45° orientation of the final fracture surface with respect to the axial direction, shear localization is considered as the dominant mechanism of plastic localization.

7. Secondary voids nucleate within the band of localized plastic deformation. The secondary voids eventually coalesce and create a macroscopic crack, independent of the microcracks associated with the necklace mechanism.

Among all steps involved in the ductile fracture process, we consider the localization of deformation in a narrow band as the most important precursor at the macroscopic level before cracks are formed at the grain level. It is worth noting that already more than 30 years ago, researchers considered shear localization as the

dominant mechanism leading to fracture of metals (e.g. Rice, 1976, [151]). On the other hand, the role of void growth and void shape changes appears to be secondary. These effects are probably only important within the band of localized deformation where other material heterogeneities (grain anisotropy and grain boundaries) may also come into play.

6.5 Conclusion

Damage mechanisms responsible for ductile failure of the TRIP steel at low strain rate have been characterized. Selected experiments, covering all the range of biaxial stresses, are carried out and interrupted at different levels of deformation. Samples extracted from the deformed specimens are analyzed by means of Optical and Scanning Electron Microscopy in order to identify the evolution of damage mechanisms. Observations show that interfaces between ferrite and martensite grains constitute preferred sites for void nucleation, which occurs at relatively low strains. However, void growth is not significant for all stress states considered. Damage increases mostly through nucleation of new cavities during deformation. It is found that the critical mechanism leading to fracture is a localization of the plastic flow at the grain scale into a planar band of shear deformation.